Space-Time Enriched Finite Elements for Elastodynamic Wave Propagation

Kieran Quaine[1,2,3*] and Heiko Gimperlein[1,4]

[1]Engineering Mathematics, Leopold-Franzens-Universität Innsbruck, Technikerstraße 13, Innsbruck, 6020, Austria.
[2]Maxwell Institute for Mathematical Sciences and School of Mathematics, Edinburgh University, James Clerk Maxwell Building, Edinburgh, EH9 3FD, United Kingdom.
[3]FEN Research GmbH, Technikerstraße 1/3, 6020, Innsbruck, Austria.
[4]Department of Mathematical, Physical and Computer Sciences, University of Parma, Parco Area delle Scienze, 53/A, 43124, Parma, Italy.

*Corresponding author(s). E-mail(s): Kieran.Quaine@fen-research.org;
Contributing authors: Heiko.Gimperlein@uibk.ac.at;

Abstract

This article investigates a generalised finite element method for time-dependent elastic wave propagation, based on plane-wave enrichments of the approximation space. The enrichment in both space and time allows good approximation of oscillatory solutions even on coarse mesh grids and for large time steps. The proposed method is based on a discontinuous Galerkin discretisation in time and conforming finite elements in space. Numerical experiments study the stability and accuracy and confirm significant reductions of the computational effort required to achieve engineering accuracy.

Keywords: Generalized Finite Element Methods, Space-Time Methods, Elastodynamics

1 Introduction

Generalised finite elements based on plane-wave basis functions have been shown since the late 1990s to significantly reduce the computational cost for the numerical approximation of wave emission and scattering problems in the frequency domain [1–7]. The enrichment of the approximation space by plane waves allows good approximation of oscillatory solutions even on coarse mesh grids whereas standard methods are limited by the need for both fine meshes and proportionally small time steps. In recent years generalizations of these methods to time-dependent problems have attracted interest, limited by the small time steps required in standard time stepping schemes [8–11]. In this work we initiate the study of generalized finite element methods for linear elastodynamics based on enrichments in both space and time. Our formulation introduces travelling plane-wave enrichments into a common finite element formulation, see e.g. [12]: We consider a time stepping scheme based on discontinuous Galerkin approximations in time and conforming finite elements in space. The numerical experiments achieve engineering accuracy on coarse meshes in space and with large time steps. They confirm the stability and accuracy of the proposed scheme and its significant reductions of the computational effort compared to standard h-version finite element schemes.

This work relates to recently proposed finite element methods for transient problems based on approximations which are taylored to the equation. On the one hand, these include (time-independent) enrichments of the approximation space, which have led to computationally efficient schemes for wave propagation [8–10, 13–16] and heat transfer problems [11, 17–19]. On the other hand, Trefftz methods based on local polynomial solutions to the considered problem [12, 20, 21] require fine meshes but reduce the computational effort with approximation spaces in each element.

In this article we build on these advances in the frequency, respectively time domain, which are based on space-only or time-only enrichments, and initiate the study of space-time enriched finite element methods for elastodynamics. Correspondingly, this new approach allows to use coarse spatial meshes and large time steps, leading to significant reductions of the number of space-time degrees of freedom required to attain a given error. The performance of the proposed method is illustrated in numerical experiments. By choosing examples closely related to those studied in previous works for time-dependent problems, we compare the benefits of the space-time enriched scheme with earlier works, as well as standard h-methods.

2 Elastic Wave Equation

Here we rewrite the initial-boundary value problem for the elastodynamic equation

$$\rho\partial_t^2\underline{u} - \mu\Delta\underline{u} - (\lambda+\mu)\nabla\left(\nabla\cdot\underline{u}\right) = F, \tag{1}$$

as a first order system in a bounded domain Ω. Including the relevant initial and boundary conditions we study the following system for the velocity $\underline{v} = \partial_t\underline{u}$:

$$\begin{cases} \dfrac{\partial\boldsymbol{\sigma}}{\partial t} - \mathbf{C}\boldsymbol{\varepsilon}(\underline{v}) = \mathbf{f}_1 \\ \rho\dfrac{\partial\underline{v}}{\partial t} - \nabla\cdot\boldsymbol{\sigma} = \underline{f}_2, \\ \underline{v}(\cdot,t_0) = \underline{v}_0,\ \boldsymbol{\sigma}(\cdot,t_0) = \boldsymbol{\sigma}_0 \quad \text{on } t = t_0 \\ \underline{v}(\underline{x},t) = \underline{g}_D \quad \text{on } \Gamma_D\times[t_0,T] \\ \boldsymbol{\sigma}(\underline{x},t)\cdot\underline{n}_x = \underline{g}_N \quad \text{on } \Gamma_N\times[t_0,T] \end{cases}. \tag{2}$$

Here, $\Gamma = \partial\Omega$ denotes the boundary, which we decompose into disjoint parts Γ_D, Γ_N, where Dirichlet (Γ_D), respectively Neumann conditions (Γ_N) are imposed. The boldfaced letters in Equation (2) denote the following tensors: $\mathbf{C}$ is the elastic coefficient tensor; $\boldsymbol{\varepsilon} = \frac{1}{2}\left(\nabla v + (\nabla v)^T\right)$ is the strain tensor, $\boldsymbol{\sigma}$ is the stress tensor and ρ the density, which we set to 1 in the following formulation. Here $F = \partial_t\underline{f}_2 + \nabla\cdot\mathbf{f}_1$. The auxiliary function $\mathbf{f}_1$ has been included to test the proposed methods for a wider variety of analytical benchmark solutions.

3 Discontinuous Galerkin Discretisation

We discretise the first order elastic systems (2). For convenience we multiply the first equation by the inverse $\mathbf{A}$ of $\boldsymbol{C}$:

$$\begin{cases} \mathbf{A}\dfrac{\partial\boldsymbol{\sigma}}{\partial t} - \boldsymbol{\varepsilon}(\underline{v}) = \mathbf{A}\mathbf{f}_1 \\ \rho\dfrac{\partial\underline{v}}{\partial t} - \nabla\cdot\boldsymbol{\sigma} = \underline{f}_2, \\ \underline{v}(\cdot,t_0) = \underline{v}_0,\ \boldsymbol{\sigma}(\cdot,t_0) = \boldsymbol{\sigma}_0 \quad \text{on } t = t_0 \\ \underline{v}(x,t) = \underline{g}_D \quad \text{on } \Gamma_D\times[t_0,T] \\ \boldsymbol{\sigma}(x,t)\cdot\underline{n}_x = \underline{g}_N \quad \text{on } \Gamma_N\times[t_0,T]. \end{cases} \tag{3}$$

For simplicity of notation, in the following we fix the initial time $t_0 = 0$. For a fixed space-time domain $\mathbf{K}$ we multiply (3) by test functions $\boldsymbol{\Theta}\in H(\mathbf{K})^{2\times 2}$, respectively $\underline{\eta}\in H(\mathbf{K})^2$, and integrate over $\mathbf{K}$ to obtain,

$$\int_{\mathbf{K}} \boldsymbol{\Theta} : \boldsymbol{A}\partial_t\boldsymbol{\sigma} - \boldsymbol{\Theta} : \boldsymbol{\varepsilon}(\underline{v}) + \underline{\eta}\cdot\partial_t\underline{v} - \underline{\eta}\cdot\left(\nabla\cdot\boldsymbol{\sigma}\right)\ \mathrm{dv} = \int_{\mathbf{K}} \boldsymbol{\Theta} : \boldsymbol{f}_1 + \underline{\eta}\cdot\underline{f}_2\ \mathrm{dv}. \tag{4}$$

We next integrate by parts in $\mathbf{K}$ to move the derivatives onto the test functions. To do so, we denote n as the outward-pointing unit normal to $\mathbf{K}$, $\underline{n}_{\mathbf{K}}$, and by n_t, $\underline{n}_x$ its temporal and spatial components. We obtain

$$\begin{aligned} &- \int_{\mathbf{K}} \boldsymbol{\sigma} : (\boldsymbol{A}\partial_t \boldsymbol{\Theta} - \boldsymbol{\varepsilon}(\underline{\eta})) + \underline{v} \cdot (\partial_t \underline{\eta} - \mathrm{div}\boldsymbol{\Theta}) \ \mathrm{dv} \\ &\quad + \int_{\partial \mathbf{K}} \boldsymbol{\sigma} : \boldsymbol{A}\boldsymbol{\Theta} n_t + \underline{v} n_t \cdot \underline{\eta} - (\boldsymbol{\sigma}\underline{n}_x) \cdot \underline{\eta} - (\boldsymbol{\Theta}\underline{n}_x) \cdot \underline{v} \ \mathrm{d}S \\ &\quad = \int_{\mathbf{K}} \boldsymbol{\Theta} : \boldsymbol{f}_1 + \underline{\eta} \cdot \underline{f}_2 \ \mathrm{dv}. \end{aligned} \tag{5}$$

Following [12, 21], we choose a discretization $\mathcal{Q}_h = \cup\mathbf{K}$ of the space-time cylinder $\mathcal{Q} = \Omega \times [0, T]$ by disjoint prismatic elements $\mathbf{K} = \Delta \times [t_1, t_2]$, where $\cup\Delta$ is an admissible triangulation of Ω. The following notation will prove useful:

- $\mathcal{Q}_h^Q$ - Interior elements
- $\mathcal{Q}_h^{\partial\Omega}$ - Element edges where the time is fixed
- $\mathcal{Q}_h^{\Gamma_{D/N}}$ - Mesh boundary edges where Dirichlet (D), respectively Neumann (N) conditions are imposed
- $\mathcal{Q}_h^{t_0}$ - Initial time faces ($\Omega \times \{0\}$)
- $\mathcal{Q}_h^T$ - Final time faces ($\Omega \times \{T\}$)

We next sum over all space-time elements $\mathbf{K}$ and rewrite (5). It is convenient to introduce the temporal jump across a face $\Delta \times \{t_j\}$ by $[[q]] = q^+ n_t^+ + q^- n_t^-$. Then we separate the integrals into their relevant boundary terms such that,

$$\begin{aligned} &\sum_{\mathbf{K}} - \int_{\mathbf{K}} \boldsymbol{\sigma} : (\boldsymbol{A}\partial_t \boldsymbol{\Theta} - \boldsymbol{\varepsilon}(\underline{\eta})) + \underline{v} \cdot (\partial_t \underline{\eta} - \mathrm{div}\boldsymbol{\Theta}) \ \mathrm{dv} \\ &\quad + \int_{\mathcal{Q}_h^{\partial\Omega}} \boldsymbol{\sigma}^- : \boldsymbol{A}[\boldsymbol{\Theta} n_t^+ + \boldsymbol{\Theta} n_t^-] + \underline{v}^- \cdot [\underline{\eta} n_t^+ + \underline{\eta} n_t^-] \ \mathrm{ds} \\ &\quad + \int_{\mathcal{Q}_h^T} \boldsymbol{\sigma} : \boldsymbol{A}\boldsymbol{\Theta} + \underline{v} \cdot \underline{\eta} \ \mathrm{ds} - \int_{\mathcal{Q}_h^{t_0}} \boldsymbol{\sigma} : A\boldsymbol{\Theta} + \underline{v} \cdot \underline{\eta} \ \mathrm{ds} \\ &\quad - \int_{\mathcal{Q}_h^{\Gamma_D}} (\boldsymbol{\sigma}\underline{n}_x) \cdot \underline{\eta} \ + (\boldsymbol{\Theta}\underline{n}_x) \cdot \underline{v} \ \mathrm{ds} \\ &\quad - \int_{\mathcal{Q}_h^{\Gamma_N}} (\boldsymbol{\sigma}\underline{n}_x) \cdot \underline{\eta} \ + (\boldsymbol{\Theta}\underline{n}_x) \cdot \underline{v} \ \mathrm{ds} = \sum_{\mathbf{K}} \int_{\mathbf{K}} \boldsymbol{\Theta} : \boldsymbol{f}_1 + \underline{\eta} \cdot \underline{f}_2 \ \mathrm{dv}, \end{aligned} \tag{6}$$

where we can then apply any boundary conditions in the formulation to get the weak formulation of the problem for $(\underline{v}, \boldsymbol{\sigma})$,

$$\begin{aligned}
&\sum_{\mathbf{K}} - \int_{\mathbf{K}} \boldsymbol{\sigma} : (\boldsymbol{A}\partial_t \boldsymbol{\Theta} - \boldsymbol{\varepsilon}(\underline{\eta})) + \underline{v} \cdot (\partial_t \underline{\eta} - \mathrm{div}\boldsymbol{\Theta}) \ \mathrm{dv} \\
&\quad + \int_{\mathcal{Q}_h^{\partial\Omega}} \boldsymbol{\sigma}^- : \boldsymbol{A}[\boldsymbol{\Theta} n_t^+ + \boldsymbol{\Theta} n_t^-] + \underline{v}^- \cdot [\underline{\eta} n_t^+ + \underline{\eta} n_t^-] \ \mathrm{ds} \\
&\quad + \int_{\mathcal{Q}_h^T} \boldsymbol{\sigma} : \boldsymbol{A}\boldsymbol{\Theta} + \underline{v} \cdot \underline{\eta} \ \mathrm{ds} - \int_{\mathcal{Q}_h^{t_0}} \boldsymbol{\sigma} : A\boldsymbol{\Theta} + \underline{v} \cdot \underline{\eta} \ \mathrm{ds} \\
&\quad - \int_{\mathcal{Q}_h^{\Gamma_D}} (\boldsymbol{\sigma}\underline{n}_x) \cdot \underline{\eta} \ \ \mathrm{ds} - \int_{\mathcal{Q}_h^{\Gamma_N}} (\boldsymbol{\Theta}\underline{n}_x) \cdot \underline{v} \ \mathrm{ds} \\
&\quad = \sum_{\mathbf{K}} \int_{\mathbf{K}} \boldsymbol{A}\boldsymbol{\Theta} : \boldsymbol{f}_1 + \underline{\eta} \cdot \underline{f}_2 \ \mathrm{dv} + \int_{\mathcal{Q}_h^{\Gamma_D}} (\boldsymbol{\Theta}\underline{n}_x) \cdot \underline{g}_D \ \ \mathrm{ds} + \int_{\mathcal{Q}_h^{\Gamma_N}} \underline{g}_N \cdot \underline{\eta} \ \mathrm{ds},
\end{aligned} \tag{7}$$

for all $(\underline{\eta}, \boldsymbol{\Theta})$ with the specified boundary data.

3.1 Discretisation

Our proposed space-time enriched methods for the elastodynamic system rely on enriched ansatz and test spaces related to those seen in standard enriched methods. They augment the standard polynomial approximation spaces by plane-wave functions in space and time, motivated by Trefftz and space-enriched methods for elastodynamic problems [12, 15]. We consider the basis functions multiplied by global enrichment functions $G(\underline{x}, t, \omega)$,

$$\underline{v}_h(\underline{x}, t) = \sum_{i}^{N} \sum_{m}^{\tilde{T}} \sum_{\underline{\kappa}} \underline{V}_m^{i\underline{\kappa}} \Pi(t)_m \Lambda_i(\underline{x}) G_{\underline{\kappa}}^m(\underline{x}, t, \omega), \tag{8a}$$

$$\bar{\underline{\eta}}_h(\underline{x}, t) = \underline{X}^{\tilde{\kappa}} \Pi(t)_m \Lambda_j(\underline{x}) \bar{G}_{\tilde{\underline{\kappa}}}^m(\underline{x}, t, \omega), \tag{8b}$$

for piecewise linear polynomial shape functions in space (Λ) and piecewise constants shape functions in time (Π). Here a tilde denotes the test function parameters, analogous to those in the ansatz (8a). We set the enrichment functions $G(\underline{x}, t, \omega)$ as plane-wave enrichments

$$G_{\underline{\kappa}}^m(\underline{x}, t, \omega) = \exp(i(\underline{\kappa} \cdot \underline{x} + \omega(t - t_m))) \quad \text{for} \quad \underline{\kappa} = (\kappa_x, \kappa_y) \in \mathbb{R}^2, \quad \omega \in \mathbb{R}, \tag{9}$$

such that the vectors $\underline{\kappa} = (\kappa_x, \kappa_y) \in \mathbb{R}^2$ lie in a lattice with

$$-\mathcal{K} \leq \kappa_x, \ \kappa_y \leq \mathcal{K}. \tag{10}$$

Equation (9) again corresponds to choosing a square of side length $2\mathcal{K}$. Note that p-waves with their longer wavelength are better resolved than s-waves with this choice of enrichments.

In order to allow real-valued numerical solutions, for every (κ, ω) we must also include $(-\kappa, -\omega)$. In this case both $G^m_{\underline{\kappa}}$ and its complex conjugate $\overline{G}^m_{\underline{\kappa}} = G^m_{-\underline{\kappa}}$ are used as enrichments, and the ansatz space in (8) contains real-valued functions.

3.2 Reduced Enriched Basis

For the elastodynamic equations we know that waves of wave speed c_p correspond to compression waves with velocity $\underline{v}$ parallel to the direction of propagation, while waves of wave speed c_s correspond to velocities $\underline{v}$ perpendicular to the direction of propagation. The general solution to the elastodynamic equation is a superposition of these. We may therefore choose the relevant velocities of the plane-wave enrichment in agreement with the direction of the vectors $\underline{V}^{i\underline{\kappa}}_m$, respectively $\underline{X}^{\tilde{\kappa}}$ in (9).

To be specific, the following functions define exact plane-wave solutions to the elastodynamic equations:

$$\underline{v}_p = \underline{\kappa} G^m_{\underline{\kappa}}(\underline{x}, t, \omega_p) = [\kappa_1, \kappa_2]\, G(\underline{x}, t, \omega_p), \tag{11}$$

$$\underline{v}_s = \underline{\kappa}^{\perp} G(\underline{x}, t, \omega_s) = [-\kappa_2, \kappa_1]\, G(\underline{x}, t, \omega_s), \tag{12}$$

where $\omega_{s/p} = c_{s/p}|\underline{\kappa}|$. The stress tensor $\boldsymbol{\sigma}_{p/s}$ corresponding to $\underline{v}_{p/s}$ is calculated from $\dfrac{\partial \boldsymbol{\sigma}_{p/s}}{\partial t} = \mathbf{C}\boldsymbol{\varepsilon}(\underline{v}_{p/s})$:

$$\begin{aligned} \boldsymbol{\sigma}_p &= \begin{pmatrix} \lambda|\underline{\kappa}|^2 + 2\mu\kappa_1^2 & 2\mu\kappa_1\kappa_2 \\ 2\mu\kappa_1\kappa_2 & \lambda|\underline{\kappa}|^2 + 2\mu\kappa_2^2 \end{pmatrix} G^m_{\underline{\kappa}}(\underline{x}, t, \omega_p), \\ \boldsymbol{\sigma}_s &= \begin{pmatrix} -2\mu\kappa_1\kappa_2 & \mu(\kappa_1^2 - \kappa_2^2) \\ \mu(\kappa_1^2 - \kappa_2^2) & -2\mu\kappa_1\kappa_2 \end{pmatrix} G^m_{\underline{\kappa}}(\underline{x}, t, \omega_s). \end{aligned} \tag{13}$$

Note the reduction of degrees of freedom compared to independent plane-wave enrichments for all components of $\underline{v}$ and $\boldsymbol{\sigma}$ leading to improved condition numbers of the finite element equations.

3.3 Stabilised Discrete Formulation

In addition, we include a stabilisation term to ensure coercivity, following the Galerkin Least Squares approach in [21],

$$\sum_{\mathbf{K}} \int_{\mathbf{K}} \hat{\mu}_1 \left(\partial_t \boldsymbol{\sigma}_h - \boldsymbol{C}\boldsymbol{\varepsilon}(\underline{v}_h)\right) \left(\partial_t \boldsymbol{\Theta}_h - \boldsymbol{C}\boldsymbol{\varepsilon}(\underline{\eta}_h)\right) + \hat{\mu}_2 \left(\partial_t \underline{v}_h - \nabla \cdot \boldsymbol{\sigma}_h\right) \left(\partial_{\underline{\eta}_h} - \nabla \cdot \boldsymbol{\Theta}_h\right) \mathrm{dv}. \tag{14}$$

As a result the enriched discretised space-time formulation becomes,

$$\begin{aligned}
&\sum_{\mathbf{K}} \Big[- \int_{\mathbf{K}} \boldsymbol{\sigma}_h : (\boldsymbol{A}\partial_t \boldsymbol{\Theta}_h - \boldsymbol{\varepsilon}(\underline{\eta}_h)) + \underline{v}_h \cdot (\partial_t \underline{\eta}_h - \mathrm{div}\boldsymbol{\Theta}_h) \ \mathrm{dv} \\
&\quad + \int_{\mathbf{K}} \hat{\mu}_1 \left(\partial_t \boldsymbol{\sigma}_h - \boldsymbol{C}\boldsymbol{\varepsilon}(\underline{v}_h)\right) \left(\partial_t \boldsymbol{\Theta}_h - \boldsymbol{C}\boldsymbol{\varepsilon}(\underline{\eta}_h)\right) + \hat{\mu}_2 \left(\partial_t \underline{v}_h - \nabla \cdot \boldsymbol{\sigma}_h\right) \left(\partial \underline{\eta}_h - \nabla \cdot \boldsymbol{\Theta}_h\right) \ \mathrm{dv} \Big] \\
&\quad + \int_{\mathcal{Q}_h^{\partial\Omega}} \boldsymbol{\sigma}_h^- : \boldsymbol{A}[\boldsymbol{\Theta}_h n_t^+ + \boldsymbol{\Theta}_h n_t^-] + \underline{v}_h^- \cdot [\underline{\eta}_h n_t^+ + \underline{\eta}_h n_t^-] \ \mathrm{ds} \\
&\quad + \int_{\mathcal{Q}_h^T} \boldsymbol{\sigma}_h : \boldsymbol{A}\boldsymbol{\Theta}_h + \underline{v}_h \cdot \underline{\eta}_h \ \mathrm{ds} - \int_{\mathcal{Q}_h^{t_0}} \boldsymbol{\sigma}_h : A\boldsymbol{\Theta}_h + \underline{v}_h \cdot \underline{\eta}_h \ \mathrm{ds} \\
&\quad - \int_{\mathcal{Q}_h^{\Gamma_D}} (\boldsymbol{\sigma}_h \underline{n}_x) \cdot \underline{\eta}_h \ \ \mathrm{ds} - \int_{\mathcal{Q}_h^{\Gamma_N}} (\boldsymbol{\Theta}_h \underline{n}_x) \cdot \underline{v}_h \ \mathrm{ds} \\
&\quad = \sum_{\mathbf{K}} \int_{\mathbf{K}} \mathbf{A}\boldsymbol{\Theta}_h : \boldsymbol{f}_1 + \underline{\eta}_h \cdot \underline{f}_2 \ \mathrm{dv} + \int_{\mathcal{Q}_h^{\Gamma_D}} (\boldsymbol{\Theta}_h \underline{n}_x) \cdot \underline{g}_D \ \ \mathrm{ds} + \int_{\mathcal{Q}_h^{\Gamma_N}} \underline{g}_N \cdot \underline{\eta}_h \ \mathrm{ds},
\end{aligned} \tag{15}$$

This leads to a time stepping scheme,

$$(\mathcal{A} + \mathcal{M}^+ + \mathcal{S} + \Gamma) \begin{pmatrix} \mathbf{v}|_{t_m} \\ \boldsymbol{\sigma}_h|_{t_m} \end{pmatrix} = \mathcal{B} - \mathcal{M}^- \begin{pmatrix} \mathbf{v}|_{t_{m-1}} \\ \boldsymbol{\sigma}_h|_{t_{m-1}} \end{pmatrix}, \quad m = 1, 2, 3, \ldots, \tag{16}$$

for $t_0 = 0$. Here the matrices are constructed using the following terms:

- Convection matrix, $\mathcal{A}$, associated to the bilinear form

  $\sum_{\mathbf{K}} - \int_{\mathbf{K}} \boldsymbol{\sigma}_h : (\boldsymbol{A}\partial_t \boldsymbol{\Theta}_h - \boldsymbol{\varepsilon}(\underline{\eta}_h)) + \underline{v}_h \cdot (\partial_t \underline{\eta}_h - \mathrm{div}\boldsymbol{\Theta}_h) \ \mathrm{dv},$
- Mass matrices, $\mathcal{M}_{t_m}^{\pm}$, corresponding to the diagonal $(+)$ and first sub-diagonal $(-)$ blocks of the space-time mass matrix associated to

  $\int_{\mathcal{Q}_h^{\partial\Omega}} \boldsymbol{\sigma}_h^- : \boldsymbol{A}[\boldsymbol{\Theta}_h n_t^+ + \boldsymbol{\Theta}_h n_t^-] + \underline{v}_h^- \cdot [\underline{\eta}_h n_t^+ + \underline{\eta}_h n_t^-] \ \mathrm{ds},$
- Stabilisation matrix, $\mathcal{S}$, associated to

  $\int_{\mathbf{K}} \hat{\mu}_1 \left(\partial_t \boldsymbol{\sigma}_h - \boldsymbol{C}\boldsymbol{\varepsilon}(\underline{v}_h)\right) \left(\partial_t \boldsymbol{\Theta}_h - \boldsymbol{C}\boldsymbol{\varepsilon}(\underline{\eta}_h)\right) +$
  $\hat{\mu}_2 \left(\partial_t \underline{v}_h - \nabla \cdot \boldsymbol{\sigma}_h\right) \left(\partial \underline{\eta}_h - \nabla \cdot \boldsymbol{\Theta}_h\right) \ \mathrm{dv},$

as well as a matrix Γ resulting from the Neumann and Robin boundary conditions. Note that with the choice of the basis (9) the matrices $\mathcal{M}_{t_j}^{\pm}$ are independent of the time step t_j, due to the shift $t - t_m$ in the time variable.

Note that with our choice of enrichment functions all matrices in (16) are independent of the time step. In the following we write $\underline{\mathbf{u}} = \left(\underline{v}_{t_m}, \boldsymbol{\sigma}_{t_m}\right)^T$, leading to the formulation

$$(\mathcal{A} + \mathcal{M}^+ + \mathcal{S} + \Gamma)\underline{\mathbf{u}}_{t_m} = \mathcal{B} - \mathcal{M}^- \underline{\mathbf{u}}_{t_{m-1}}, \quad m = 1, 2, 3, \ldots. \tag{17}$$

4 Numerical Experiments

The numerical experiments solve the stabilised discrete formulation (15) with Neumann boundary conditions imposed on $\Gamma = \Gamma_N$.

We choose the stabilisation parameters, $\mu_1 = \mu_2$, such that

$$\mu_1 = \mu_2 = \sup_{(\underline{x},t)\in\mathbf{K}} |(\underline{x},t) - (\underline{x}_c,t_c)|/\max(\mathcal{K})^2, \tag{18}$$

where the $\max(\mathcal{K})^2$ accounts for the two-dimensional enrichments and $(\underline{x}_c,t_c)$ are the spatial and temporal centre of the element. For the numerical evaluation of the integrals in (15), we use the symbolic integration package in *MATLAB* [22] to obtain exact analytical formulas for the entries of all matrices. A standard Gauss quadrature is used for the numerical integration of the right-hand side, see also [23, 24] for a detailed description of numerical quadrature techniques for oscillatory problems.

The resulting linear system in each time step is solved using the standard backslash command in *MATLAB*. The study of preconditioned iterative solvers, as for time-independent problems [25], is beyond the scope of the current work.

In the numerical results we will often use the notation $\{\kappa\}$ for the total number of wave vectors κ used in a given computation. Here we note that the total number of enrichments depends on the chosen set of wavenumbers and frequencies. In our experiments unless specified otherwise we choose the frequencies $\omega = \pm c_{p/s}|\kappa|$, where $c_{p/s}$ are the two wave speeds, so that the total number of space-time enrichments for each wave speed is given by

$$\{\kappa\} = 2(2\mathcal{K}+1)^2 - 1. \tag{19}$$

Computation of L^2-errors

The accuracy of the obtained numerical results is quantified using absolute or relative L^2 errors in space-time, respectively in space L^2 error in space or space-time. To be specific, denote by $v(\underline{x},t)$ the exact solution to (2) (or a benchmark), and by $v_h(\underline{x},t)$ the approximate solution obtained from (15). Then the corresponding space-time L^2 norm $||v - v_h||_{L^2(\Omega\times[0,T])}$ of the error is denoted by $||v - v_h||_{L^2}$. We evaluate this norm using numerical quadrature:

$$\begin{aligned} ||v(\underline{x},t) - v_h(\underline{x},t)||^2_{L^2} &= \sum_{\mathbf{K}} \int_{\mathbf{K}} |v(\underline{x},t) - v_h(\underline{x},t)|^2 \mathrm{d}V, \\ \int_{\mathbf{K}} |v(\underline{x},t) - v_h(\underline{x},t)|^2 \ \mathrm{dv} &\simeq \sum_{i,j} w_j\omega_i |v(\underline{x}_i,t_j) - v_h(\underline{x}_i,t_j)|^2. \end{aligned} \tag{20}$$

Here ω_i denote the weights, $\underline{x}_i$ the nodes of the numerical quadrature in space [24, 26], while w_j denote the weights, t_j the nodes of the numerical quadrature in time. Similarly, we compute relative errors as

$$\frac{||v(\underline{x},t) - v_h(\underline{x},t)||_{L^2}}{||v(\underline{x},t)||_{L^2}} \simeq \frac{\sum_{\mathbf{K}} \sum_{i,j} \omega_i w_j |v(\underline{x}_i,t_j) - v_h(\underline{x}_i,t_j)|^2}{\sum_{\mathbf{K}} \sum_{i,j} \omega_i |u(\underline{x}_i,t_j)|^2}. \tag{21}$$

The numerical approximation of the spatial L^2 norm $||v - v_h||_{L^2(\Omega)}$ of the error at a fixed time t is analogous, involving only numerical quadrature in space:

$$||v(\underline{x},t) - v_h(\underline{x},t)||^2_{L^2(\Omega)} \simeq \sum_{\Delta} \sum_{i} \omega_i |v(\underline{x}_i,t) - v_h(\underline{x}_i,t)|^2. \tag{22}$$

4.1 P-Wave Propagation

In this example we compare the simple choice of enrichment functions from Section 3.1 to the enrichment by p- and s-waves from Section 3.2. Consider the domain $\Omega = [0, 2\pi]^2$ and the exact solution

$$\underline{v}(\underline{x},t) = [\sin^2(t)(\cos(\kappa x + \omega t) + 0.57\cos(2\kappa x - 2\omega t)), 0], \tag{23}$$

with corresponding stress defined by

$$\boldsymbol{\sigma} = \int_{t_0}^{t} \boldsymbol{C} : \boldsymbol{\varepsilon}\underline{v}(\underline{x},s) + \boldsymbol{f}_1(\underline{x},s)\ \mathrm{ds}, \tag{24}$$

taken from (2). The elastic coefficients are given by $\lambda = 1$ and $\mu = \frac{1}{3}$.

We use $\kappa = 1$ with $\omega = \sqrt{2}$, a stability constant $\mu_1 = 10^{-6}$ and note that the initial condition is 0 at $t = 0$. A result of the simple nature of the solution, it will be sufficient to consider the error in the first component of the velocity.

We choose enrichments as in Section 3.1 and include the exact wavenumber leading to the expectation of a high degree of accuracy with a small number of degrees of freedom.

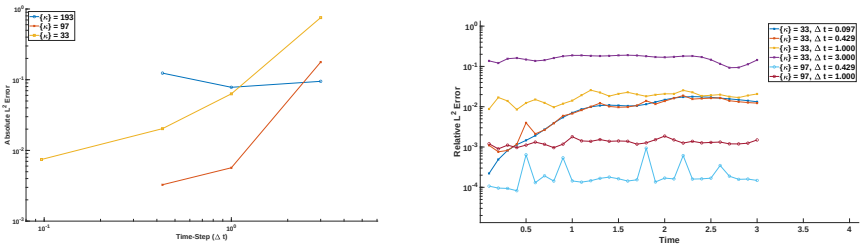

(a) (b)

Fig. 1: L^2 space errors against the time step (1a) and over time (1b) at $t = 0.5$.

We see from Figures 1a and 1b that the enriched schemes work as we saw in the acoustic system. Now recalling that the problem specified $\kappa = 1$ which means we have a wavenumber of 1 and 2 then we will be able to approximate the problem using both enrichments including these wavenumbers. As a result we see that for when we use the enrichment $\mathcal{K} = 1$ and $\mathcal{K} = 2$ (33 and 97) we are satisfying part of the exact solution, thus giving us a reasonable approximation of the result. One issue we encounter are stability issues due to the almost linearly dependent basis functions when using 4 different temporal frequencies for a small time step, with resulting poor approximation for $\mathcal{K} = 3$ (193). These problems are further emphasised when we consider $\Delta t \approx 0.5$ and 97 enrichments. We observe spikes in the time interval studied here, related to an increase in the conditioning when adding more enrichments. While the coefficient vector is typically poorly approximated, the resulting solution (after post-processing) often remains accurate. At special times, though, floating point errors in the post-processing may randomly reduce the accuracy of the solution. As we can see in Figure 1b the best performing enriched scheme is when we have set $\mathcal{K} = 2$ as we see it stays around the level of a 10^{-4} error throughout the time frame for $\Delta t \approx 0.5$ whereas, as we would expect, the error is larger for the larger steps on this problem but again it is consistent. However, we see a different story for when we take the enrichment $\mathcal{K} = 1(33)$ over time. We see that the smallest time step $\Delta t \approx 0.1$ starts off with a comparable error to $\mathcal{K} = 2(97)$ but has a steady rise over the time frame from 10^{-4} before levelling out at 10^{-2}. This is an example of the enrichment approximating the initial times well, due to the effect of the larger wavenumber being negligible due to the prefactors associated with it. We also see from this plot that when we increase the number of enrichments to $\mathcal{K} = 3$ we often see that the solution exhibits blow up, noting the cut-off, due to conditioning issues with respect to the time step. As a result we see that for small times, we can approximate the solution well before the conditioning becomes untenable unless we have a large time step, such as $\Delta t = 3$. To counteract the singularity issue, we discussed in Section 3.2 that changing the basis functions will have a profound affect on the errors associated with the problem.

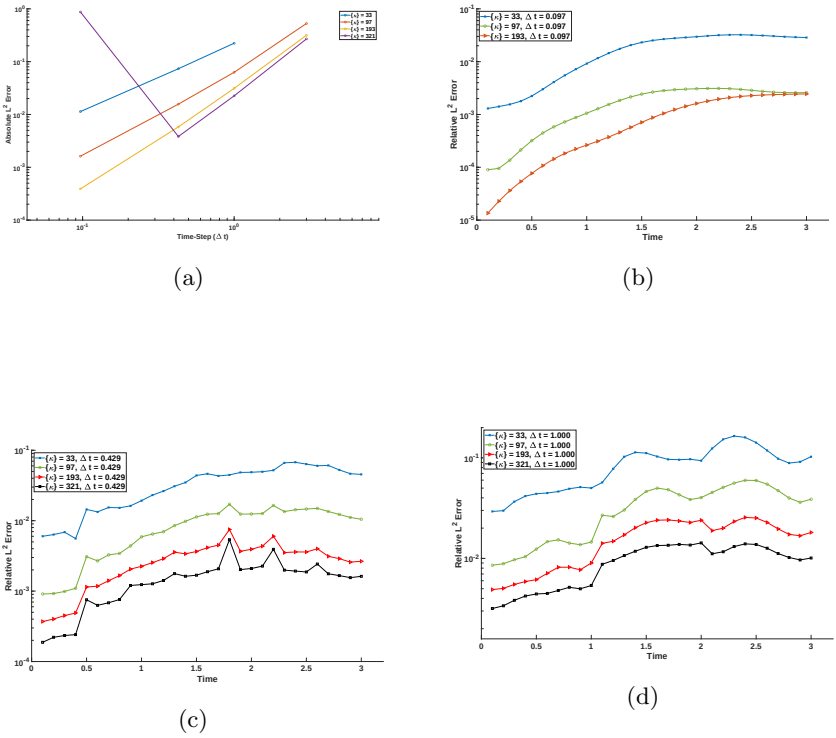

Fig. 2: L^2 space errors against the time step (2a) and over time (2b - 2d) with varying time steps at $t = 0.5$.

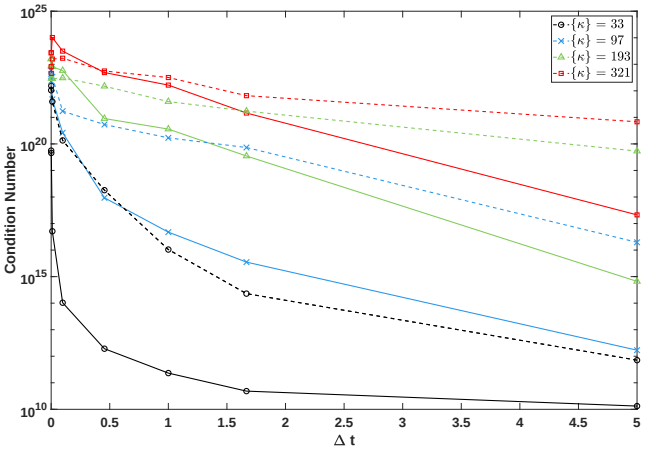

Fig. 3: Condition numbers vs. time step for different enrichments (dashed lines: enrichments (9), solid lines: enrichments (11) - (13)).

In Figure 2 we observe convergence in the enrichments compared to associated time steps, as we see for 33, 97 and 193 ($\mathcal{K} = 1, 2, 3$), where there is a stable decrease in the absolute error but we still exhibit the same behaviour as before when we push the enrichments further leading to singularities and blow up for small time steps, although we are able to increase the total number of enrichments with this reduction in the basis. This blow up behaviour is related to conditioning in Figure 3, where the condition number is shown depending on the size of the time step. We see that the condition number, and therefore the stability of the method, improves with increasing time step. As long as the time step is large enough and therefore the condition number sufficiently small, however, Figures 2 show that a reduction of the time step leads to a smaller error, because the error of the time discretization decreases. For fixed enrichments we therefore observe an optimal intermediate regime for the time step which balances the errors due to ill-conditioning and time discretization. The upcoming experiments confirm these results, and an in-depth investigation of the relationship between enrichments, time step and mesh size will be the topic of future work.

For the following experiments we only consider the enrichments defined by p- and s-waves, with no stabilisation term in the bilinear form.

4.2 Trailing Wave Propagation

In this experiment we will be considering a wavefront solution with a trailing edge and a cut off. To do this we define the exact solution for the velocity such

that,

$$\underline{v}(\underline{x},t) = \begin{cases} [\cos^2(\kappa(x - x_0 - c_p t)), 0] & \text{for } \kappa(x - x_0 - c_p t) < \pi/2 \\ 0 \end{cases} \tag{25}$$

where the corresponding solutions for the stress can be computed using the homogenous version of (3) yielding the required traction. Here we define κ as the wavenumber, c_p as the p-wave speed and x_0 as the starting crest of the wave. We further define the solution on a square over $[0, 2\pi]^2$, as before, and let $(\lambda, \mu) = (1, \frac{1}{2})$; $c_p = \sqrt{2}$; $\kappa = 2$, $x_0 = -\frac{3\pi}{4}$ and $t \in [0, 3]$ to ensure the wave travels through the domain. As a result, we expect to see that the wave will travel from left to right with the initial times being zero in the domain until the wavefront hits the boundary at $t \approx 1.11$. Now we look to solve this using both a standard finite element method as well as the space-time enriched scheme developed in this chapter. To do this we define the enriched mesh to be a uniform 4×4 triangular grid and then define the enrichments to be in the set $\mathcal{K} \in 1, 2, 3, 4$ with the frequencies set to $\omega = \pm (c_p, c_s) |\mathcal{K}|$ for the relevant enrichments and $\mu_1 = 0$. As a result we would expect to see that the approximations become more accurate as we increase the number of enrichments, noting that the frequency is attained for $\mathcal{K} = 4$ by a simple rewriting of exact solution.

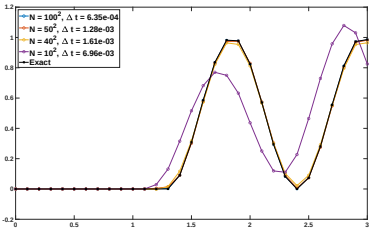

(a) h-method

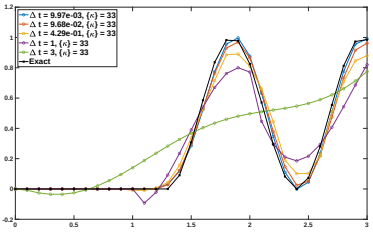

(b) $\mathcal{K} = 1$

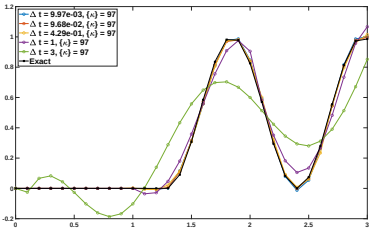

(c) $\mathcal{K} = 2$

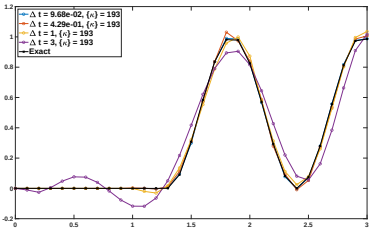

(d) $\mathcal{K} = 3$

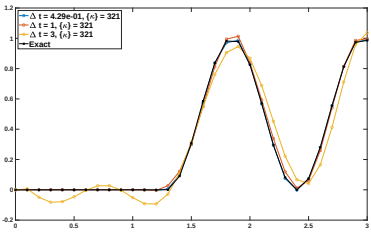

(e) $\mathcal{K} = 4$

Fig. 4: Cross sections over time for the point $(x, y) = (0.256, 2.821)$ against the exact solution (black).

Now if we consider the following cross-section plots at $(x, y) = (0.256, 2.821)$ over time for the h-method (Figure 4a) and an enriched scheme (Figures 4b-4e) we see that there is clear convergence in the h-method as we increase the number of nodes in the the system, as is reasonable expected. Now if we consider the enriched method then we see that for $\Delta t < 0.5$ and $\mathcal{K} = 1$ (33), 2 (97), and 3 (193) we get reasonable approximations of the solution, even for the short times. However, if we consider the converse case - when $\Delta t > 0.5$ - then we see that for $\mathcal{K} = 1$ we have poor results, which does not accurately reproduce the system we are solving whereas for $\mathcal{K} = 2$ (97), 3 (193), and 4 (321) we see that the solution is matched well qualitatively over the system except for short times with larger time steps. This is seen for the largest steps in all of the plots, for example if we consider $\Delta t = 3$ then we will struggle to approximate 0 due to the large jumps over the domain, whereby we have not attained enough information about the given system to truly approximate a short and stationary (in the domain) solution. This however, changes somewhat - qualitatively - when the wavefront hits the boundary as the enrichment is then able to capture some of the behaviour, even if it is out of phase. Combining the above we see that as we increase the number of enrichments with a sufficiently small time step we are able to approximate the solution well, noting that particularly good qualitative results are obtained for a range $\{\kappa\} = 97,\ 193,\ 321$ of enrichments, with $\Delta t = 9.97 \times 10^{-3},\ 9.98 \times 10^{-2},\ 4.29 \times 10^{-1}$ respectively. To quantify the accuracy we compute the relative L^2 errors in space for the first component of velocity using the exact solution (25).

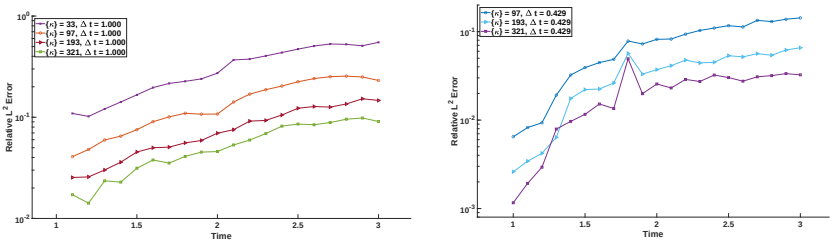

(a) $\Delta t = 1$ (b) $\Delta t = 0.5$

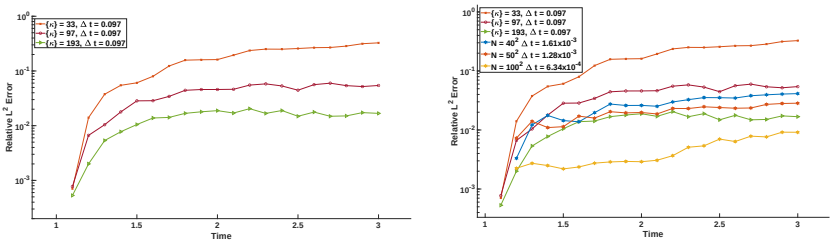

(c) $\Delta t = 0.097$ (d) H Method

Fig. 5: Relative L^2 errors over time for a given time step and enrichment $\mathcal{K}$.

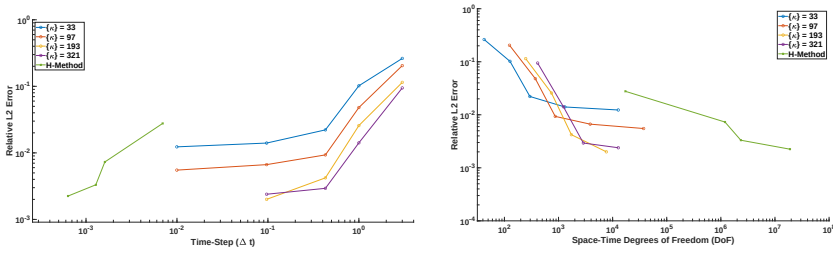

(a) (b)

Fig. 6: 6a: Relative L^2 space errors against the time step for a given number of enrichments at $t = 1.2$; 6b: Relative L^2 errors against the space-time degrees of freedom at $t = 1.2$.

Here Figure 5 shows us that the L^2 errors after the wavefront hits the boundary (noting we have removed the errors for $\delta t > 1$). We see that at the initial 'impact' the errors for the finest h method ($\star$) and the highest number of enrichments produce a small error in the initial steep or miss the initial wavefront, due to numerical errors. We see that the enriched methods tend to

perform more consistently over the full domain without much rise in the error over the scheme whereas the h-method has as steady rise over the time frame, as expected with standard schemes. If we consider Figures 6a and 6b we see both the advantages and disadvantages of the enriched method. We see a clear advantage in terms of the error compared to the time step and the space-time degrees of freedom. For example if we consider the enrichments for $\mathcal{K} = 4$ (321) we see that the errors decrease rapidly as the time step is decreased before levelling out when the enrichments either become inefficient or blow up - in this case we have removed the point at $\Delta t = 0.01$ as we experienced blow-up due to singularities, as is demonstrated for $\mathcal{K} = 3$ (193). As a result we see that the enriched schemes produce errors between 10^{-2} and 10^{-3} which are comparable to the standard finite element scheme but at a reduced computational cost, noting that the standard scheme requires a time step of 10^{-2} to 10^{-3} compared to the enriched which are all larger than 10^{-2} with the most accurate result being attained at $\Delta t = 10^{-1}$. This increased order of the time step allows for faster and in this case more accurate solutions when we compare computational costs. If we then continue to look at the degrees of freedom, we start to see a clear difference between the two methods. We observe that the computational costs associated with the enriched methods are substantially lower than the h-method, noting that to attain an error of 10^{-2} we need 10^3 space-time degrees of freedom compared to 10^{-6}. This stark difference is further emphasised when we consider $\mathcal{K} = 4(321)$ with 14^3 DoF compared to the h-method with 19×10^6 DoF which both have an error 3×10^{-3}. We can conclude that the enriched finite element schemes produces results of comparable accuracies for substantially smaller computational costs over a variety of enrichments chosen.

4.3 Impulse On a Rectangle

In this example we will be considering a sinusoidal impulse over a rectangular domain, $\Omega = [0, 24] \times [0, 6]$ with 6 elements and 8 nodes in space.

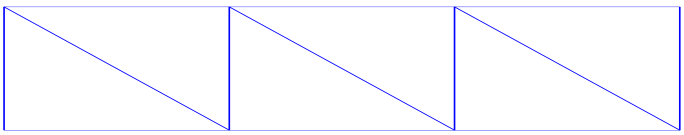

Fig. 7: Coarse rectangular mesh.

Here we would expect that we will need a high number of enrichments to account for the spatial error associated with the sparsity of the elements in

this domain. We then define the impulse to be over the domain

$$\begin{aligned} f_2^1 &= \sin(k(x+ct)) \\ f_2^2 &= \frac{\sin(k(x+ct))}{4}, \end{aligned} \tag{26}$$

where at $t = 2$ we will turn off the source term to give some more physical meaning to the problem. As a result the physical interpretation of this problem is that we expect some oscillatory impulse over the domain throughout time which could correspond, loosely, to a defect in a trains wheel for example with a kill time of the source after the 'train' has passed over the track [27]. We set the parameters for the problem such that: $k = 1$; $c = \sqrt{5}$; $\lambda = 1$; $\mu = 5$; $t \in [0, 5]$. We further let the stability parameter, $\mu_1 = 0$. The following plots demonstrate both the quantitative and qualitative approximation by the elastodynamic enrichments. We compute the spatial L^2 error compared to a benchmark solution obtained by the standard h-method with 40,000 nodes and time step $\Delta t = 0.0003$, as in Section 4.

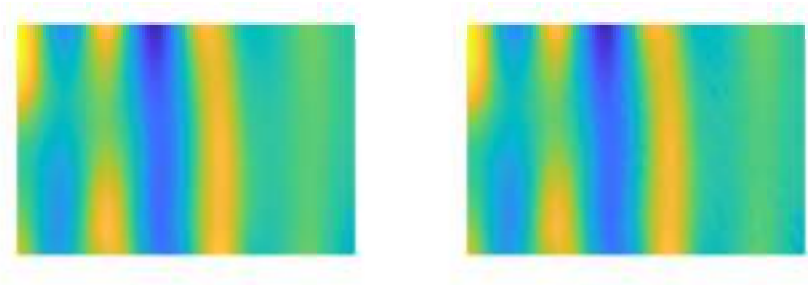

(a) Benchmark solution (b) $\mathcal{K} = 5$

Fig. 8: Here we compare the benchmark to the enriched method with 20,000 and 6 spatial nodes respectively.

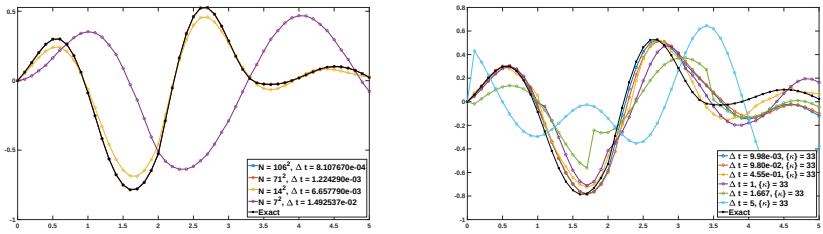

(a) h-method (b) $\mathcal{K} = 1$

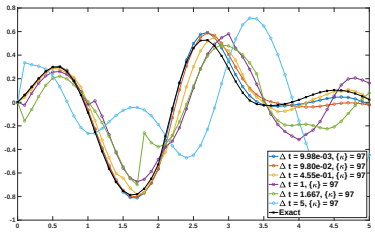

(c) $\mathcal{K} = 2$

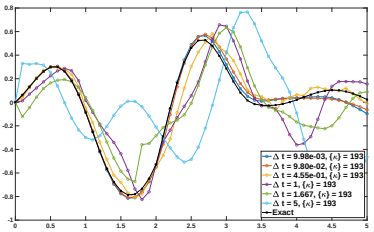

(d) $\mathcal{K} = 3$

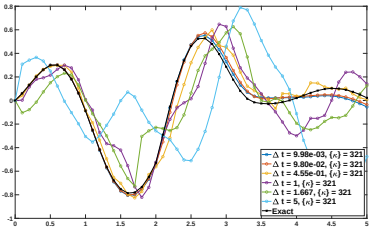

(e) $\mathcal{K} = 4$

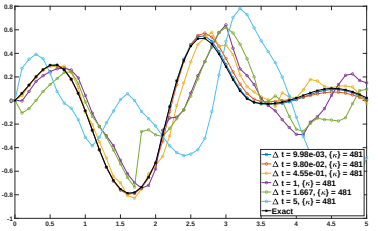

(f) $\mathcal{K} = 5$

Fig. 9: Cross sections over time for the point $(x, y) = (19.39, 0.3030)$ against the exact solution (black).

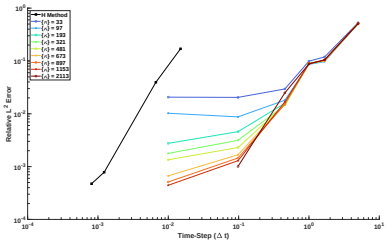

(a)

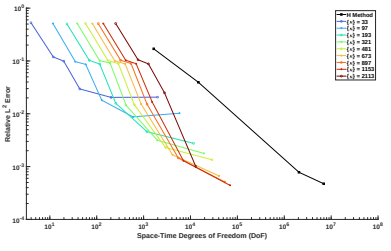

(b)

Fig. 10: Comparison of the benchmark to the enriched method with 20,000 and 6 spatial nodes respectively. 10a: Relative spatial error at $t = 0.5$ against the time step; 10b: Relative spatial error at $t = 0.5$ against the space-time degrees of freedom.

From Figure 9 the enriched methods perform well when we both increase the number of enrichments as well as decreasing the time step where we observe

a clear relationship between the time step and number of enrichments in each figure: as long as the time step is not too large, a good approximation is obtained for a sufficiently large number of enrichments. Here in Figure 8b we visually cannot see any difference between the solutions at the final time, $t = 5$. This allows us to conclude that the enrichments do qualitatively approximate the standard finite element scheme with substantially fewer spatial degrees of freedom. To further emphasise this point we now consider the cross sections solutions over time - Figure 9. Here we see that the standard finite element scheme converges as we would expect as the number of spatial nodes are increased. However, with the enriched scheme we see poorer performance for the small numbers of enrichments before seeing reasonable accuracy, at short times for $\mathcal{K} = 2$ (97) and 3 (193). As we increase the number of enrichments more and take a relatively small time step we see that the method approximates the benchmark (40,000 nodes) well throughout all times. We also see that the enrichments cater well to the cut off in the source as we see a significant reduction in the amplitude of the problem towards the end of the time period, giving more clarity to the agreement seen in Figure 8b. In addition, Figures 10a and 10b show that as we increase the number of enrichments the error decreases rapidly. Given the coarse mesh with only 6 elements, we observe a reduction of the number of degrees of freedom by 2 to 3 orders of magnitude compared to a standard h-method. We see from Figure 10b that as the space-time degrees of freedom decrease (noting that the spatial degrees of freedom is constant for the enriched method) there is a stark decrease in the relative error once we have a small enough time step to solve the system, which is evident if we consider $\Delta t > 0.5$ as all the errors lie on one another. However, we should note that as we increased the number of enrichments past 2000 (2113) we started to see conditioning issues, so have been forced to remove the final temporal point at $\Delta t = 10^{-2}$, due to blow-up, but this can be rectified by including the stability parameters discussed in Section 3.3. Therefore, key advantages that we can see here with the enriched scheme, compared to the H method, is that the errors rapidly decrease, over a small change in the degrees of freedom and that we require substantially fewer degrees of freedom - noting for 481 enrichments we required approximately two orders less to achieve comparable errors to the standard scheme. This allows us to conclude that the enriched schemes are able to capture the elastic behaviour associated with plane-wave impulses and the two differing wave speeds.

4.4 Sinusoidal Impulse

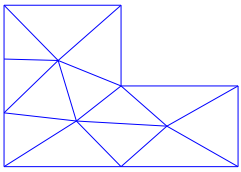

Fig. 11: Coarse L-shape mesh.

Here in this example we will be considering an L-shape domain over $\Omega \in [0, 4\pi]$ in each direction with a minimal number of nodes for the enriched scheme. The mesh we will be using (Figure 11) has 12 nodes and is a quasi-uniform mesh, by design. The reason for this is to emphasise that an enriched method can still perform well on non-uniform elements as is reasonably expected in real world applications. Now we will pose the following source terms for the velocity components for $\underline{f}_2 = (f_2^1, f_2^2)$ such that,

$$\begin{aligned} f_2^1 &= \sin(k(x+ct)) \\ f_2^2 &= \frac{\sin(k(x+ct))}{4} \end{aligned} \tag{27}$$

to ensure that we have both a p and s wave present in the solution. We set $k = \frac{1}{2}$ and $c = 1$ over the time frame $[0, 5]$, impose the Neumann conditions such that $\boldsymbol{\sigma} \cdot \underline{n} = 0$ on all boundaries and let the material parameters $\lambda = 1$ and $\mu = 5$. If we then consider this example by taking $\mathcal{K} \in [2, 3, 4, 5]$. Using these parameters we are able to obtain good qualitative approximations, shown as cross-sectional solutions in Figure 12. The relative L^2 errors in space are computed by following the definition in Section 4 and are shown in Figures 13a and 13b.

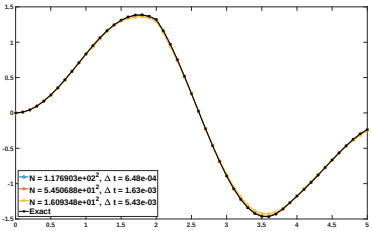

(a) h-method

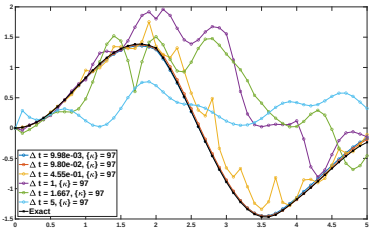

(b) $\mathcal{K} = 2$

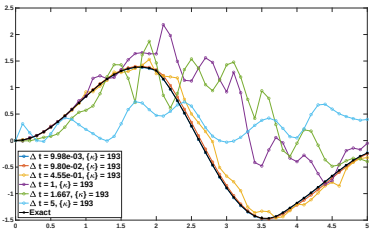

(c) $\mathcal{K} = 3$

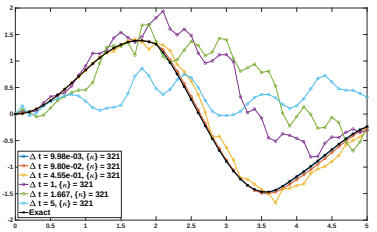

(d) $\mathcal{K} = 4$

Fig. 12: Cross sections over time for the point $(x, y) = (0, -3.391)$ against the exact solution (black).

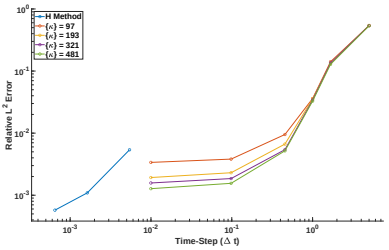

(a)

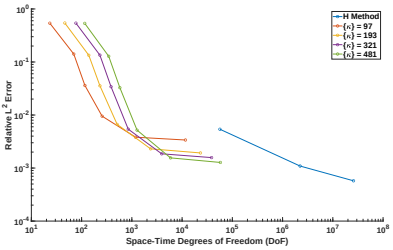

(b)

Fig. 13: Relative spatial error at $t = 0.5$ against the time step (13a) and space-time degrees of freedom (13b).

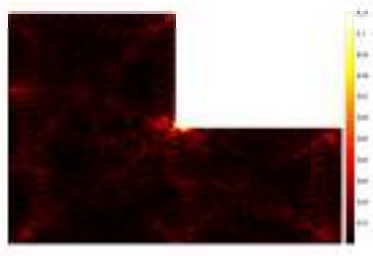

(a) $t = 1$.

(b) $t = 2$.

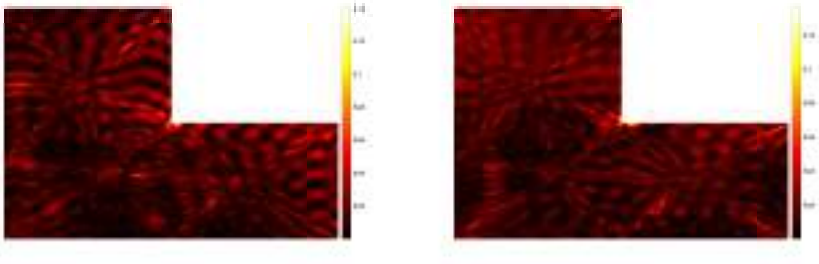

(c) $t = 4$. (d) $t = 5$.

Fig. 14: Absolute error over the L-shaped domain.

From Figure 12 the enriched methods perform well when we both increase the number of enrichments as well as decreasing the time step. In this example we see that the enriched methods appear to be indistinguishable compared to the exact solution when $\Delta t < \frac{1}{2}$ and offers evidence towards some clear convergence, where we see a clear relationship between the time step and enrichments in each figure. Consequently, we ensure that the time step is not too large then we can see a good approximation for a sufficient number of enrichments. However, for the larger time steps we do see that the numerical solution produced is rather chaotic for all of the enrichments, although we see qualitative improvements as the number of enrichments are increased. The reasoning behind this poor behaviour at large time steps, compared to our other examples is likely due to the nature of the problem where we are trying to enrich in space with plane-waves, which likely do not satisfy the solution across every element - noting a wavefront crossing an enriched element will lead to a truncation in the solution, which the enrichments are not designed to handle [28]. Consequently, we are forced to decrease the time step to obtain reliable results. To see in more detail how the enrichments fare we should consider some errors for the given problem, based on a benchmark of approximately $40,000$ nodes in space. If we now consider Figures 13a and 13b we see that the accuracy of the enriched method is comparable to a standard scheme at roughly 10^{-3} but the associated time step is at least one order larger and in most cases having a time step two orders larger produces results at the same accuracy level. Moreover, if we consider Figure 13b we see a much starker difference between the two methods. Here we see that to find the error at $t = 0.5$ we are able to attain the same error with two orders of magnitude less in the space-time domain, due to the vastly reduced spatial and temporal components we can save substantial amounts of computational effort to produce accurate results for this impulse problem. Furthermore we see from Figure 14 that the error is predominately centred around the re-entrant (note the bright colour) corner during the time frame which is likely the primary cause for the poor approximations over the domain. We also see that as time progresses that the

spatial discretisation is leading to larger errors as we start to see the errors propagating over the large elements in the enriched mesh, To counter these rises in error we would likely need to provide more specific enrichments, such as Bessel functions, around the corners to accurately deal with this scattering problem, as has been done by [28].

5 Conclusion

In this article we initiated the study of space-time enriched finite elements for elastodynamics. The approximation spaces are here enriched by travelling plane waves. Discontinuous elements in time were combined with conforming, continuous elements in space, leading to a time stepping scheme which generalizes both standard h version finite element methods and spectral methods. The numerical experiments confirm the rapid convergence of the method to engineering accuracy and quantify the significant computational savings compared to standard finite element methods. The obtained accuracies are comparable to other enriched or Trefftz methods, using a reduced number of degrees of freedom [4, 8, 9, 12]. Choosing enrichments based on travelling s and p waves and their corresponding stresses, rather than general plane waves which do not necessarily solve the elastodynamic problem, significantly improves the conditioning of the linear systems and reduced numbers of degrees of freedom.

This article provides the basis to study the optimal balance of mesh size, time step and enrichment numbers, as well as preconditioning strategies in future work.

Acknowledgements

We thank Omar Laghrouche for fruitful discussions on the topics of this article.

Declaration of Competing Interests

We would like to thank *The Maxwell Institute Graduate School in Analysis and its Applications*, a Centre for Doctoral Training funded by the UK Engineering and Physical Sciences Research Council (grant EP/L016508/01), Heriot-Watt University, University of Edinburgh and AWE (Contract no. PO30408299) for their sponsorship. The authors have no further competing interests to declare that are relevant to the content of this article

References

[1] Melenk, J.M., Babuška, I.: The partition of unity finite element method: Basic theory and applications. Computer Methods in Applied Mechanics and Engineering **139**(1), 289–314 (1996)

[2] Babuska, I., Melenk, J.M.: The partition of unity method. International Journal for Numerical Methods in Engineering **40**(4), 727–758 (1997)

[3] Laghrouche, O., Bettess, P., Astley, R.J.: Modelling of short wave diffraction problems using approximating systems of plane waves. International Journal for Numerical Methods in Engineering **54**(10), 1501–1533 (2002)

[4] Laghrouche, O., Bettess, P., Perrey-Debain, E., Trevelyan, J.: Wave interpolation finite elements for Helmholtz problems with jumps in the wave speed. Computer Methods in Applied Mechanics and Engineering **194**(2), 367–381 (2005)

[5] Perrey-Debain, E., Trevelyan, J., Bettess, P.: On wave boundary elements for radiation and scattering problems with piecewise constant impedance. IEEE Transactions on Antennas and Propagation **53**(2), 876–879 (2005)

[6] El Kacimi, A., Laghrouche, O.: Numerical modelling of elastic wave scattering in frequency domain by the partition of unity finite element method. International Journal for Numerical Methods in Engineering **77**(12), 1646–1669 (2009)

[7] Mahmood, M.S., Laghrouche, O., Trevelyan, J., El Kacimi, A.: Implementation and computational aspects of a 3d elastic wave modelling by pufem. Applied Mathematical Modelling **49**, 568–586 (2017)

[8] Drolia, M., Mohamed, M.S., Laghrouche, O., Seaid, M., Trevelyan, J.: Enriched finite elements for initial-value problem of transverse electromagnetic waves in time domain. Computers and Structures **182**, 354–367 (2017)

[9] Drolia, M., Mohamed, M., Laghrouche, O., Seaid, M., El-Kacimi, A.: Explicit time integration with lumped mass matrix for enriched finite elements solution of time domain wave problems. Applied Mathematical Modelling **77**, 1273–1293 (2020)

[10] Ham, S., Bathe, K.J.: A finite element method enriched for wave propagation problems. Computers & Structures **94-95**, 1–12 (2012)

[11] Iqbal, M., Gimperlein, H., Mohamed, M.S., Laghrouche, O.: An a posteriori error estimate for the generalized finite element method for transient heat diffusion problems. International Journal for Numerical Methods in Engineering **110**(12), 1103–1118 (2017)

[12] Barucq, H., Calandra, H., Diaz, J., Shishenina, E.: Space–time Trefftz-DG approximation for elasto-acoustics. Applicable Analysis **99**, 747–760 (2020)

[13] Gimperlein, H., Stark, D.: Algorithmic aspects of enriched time domain boundary element methods. Engineering Analysis with Boundary Elements **100**, 118–124 (2019)

[14] Antonietti, P.F., Mazzieri, I., Migliorini, F.: A space-time discontinuous galerkin method for the elastic wave equation. Journal of Computational Physics **419**, 109685 (2020) https://doi.org/10.1016/j.jcp.2020.109685

[15] Yang, Y., Chirputkar, S., Alpert, D.N., Eason, T., Spottswood, S., Qian, D.: Enriched space–time finite element method: a new paradigm for multi-scaling from elastodynamics to molecular dynamics. International Journal for Numerical Methods in Engineering **92**(2), 115–140 (2012)

[16] Destuynder, P., Hervella-Nieto, L., López-Pérez, P.M., Orellana, J., Prieto, A.: A modal-based partition of unity finite element method for elastic wave propagation problems in layered media. Computers & Structures **265**, 106759 (2022)

[17] Iqbal, M., Gimperlein, H., Laghrouche, O., Alam, K., Shadi Mohamed, M., Abid, M.: A residual a posteriori error estimate for partition of unity finite elements for three-dimensional transient heat diffusion problems using multiple global enrichment functions. International Journal for Numerical Methods in Engineering **121**(12), 2727–2746 (2020)

[18] Iqbal, M., Alam, K., Gimperlein, H., Laghrouche, O., Mohamed, M.S.: Effect of enrichment functions on gfem solutions of time-dependent conduction heat transfer problems. Applied Mathematical Modelling **85**, 89–106 (2020)

[19] Iqbal, M., Stark, D., Gimperlein, H., Mohamed, M.S., Laghrouche, O.: Local adaptive q-enrichments and generalized finite elements for transient heat diffusion problems. Computer Methods in Applied Mechanics and Engineering **372**, 113359 (2020)

[20] Moiola, A., Perugia, I.: A space–time Trefftz discontinuous Galerkin method for the acoustic wave equation in first-order formulation. Numerische Mathematik **138**(2), 389–435 (2018)

[21] Imbert-Gérard, L.-M., Moiola, A., Stocker, P.: A space–time quasi-Trefftz DG method for the wave equation with piecewise-smooth coefficients. Mathematics of Computation **92**(341), 1211–1249 (2023)

[22] MATLAB: Version 9.12.0 R2022b. The MathWorks Inc., Natick, Massachusetts (2022)

[23] Quaine, K.: Space-Time Enriched Finite Elements For Acoustic and Elastodynamic Problems. PhD Thesis, Heriot-Watt University

[24] Laghrouche, O., Bettes, P.: Short wave modelling using special finite elements. Journal of Computational Acoustics **08**(01), 189–210 (2000)

[25] El Kacimi, A., Laghrouche, O.: Wavelet based ilu preconditioners for the numerical solution by pufem of high frequency elastic wave scattering. Journal of Computational Physics **230**(8), 3119–3134 (2011)

[26] Richardson, C.L., Hegemann, J., Sifakis, E., Hellrung, J., Teran, J.M.: An xfem method for modeling geometrically elaborate crack propagation in brittle materials. International Journal for Numerical Methods in Engineering **88**(10), 1042–1065 (2011)

[27] Sheng, X., Liu, Y., Zhou, X.: The response of a high-speed train wheel to a harmonic wheel-rail force. In: Journal of Physics: Conference Series, vol. 744, p. 012145 (2016). IOP Publishing

[28] Gilvey, B., Trevelyan, J., Hattori, G.: Singular enrichment functions for helmholtz scattering at corner locations using the boundary element method. International Journal for Numerical Methods in Engineering **121**(3), 519–533 (2020)